Postprint of: Faezeh Eydi, Afsaneh Mojra and Rezvan Abdi, Comparative analysis of the flow control over a circular cylinder with detached flexible and rigid splitter plates, Journal of Physics of Fluids 34 (2022), Article 113604. https://doi.org/10.1063/5.0110398

Comparative analysis of the flow control over a circular cylinder with detached flexible and rigid splitter plates

Faezeh Eydi [1*], Afsaneh Mojra[1] and Rezvan Abdi[2]

[1] Department of Mechanical Engineering, K. N. Toosi University of Technology, Tehran, Iran
[2] Faculty of Civil and Environmental Engineering, Gdansk University of Technology, Narutowicza 11/12, 80-233 Gdansk, Poland

Emails: eydi1377@email.kntu.ac.ir, *mojra@kntu.ac.ir*, *rezvan.abdi@pg.edu.pl*

Submitted Version to Journal of Physics of Fluids

Abstract

A comparative study is performed on a circular cylinder with both flexible and rigid splitter plates (SPs). This study has the novelty of using single and dual detached SPs located downstream of the cylinder. The dimensionless gap distance between the first splitter plate and the cylinder as well as the distance between the SPs are varied. The strain of flexible SPs can be used for energy harvesting from the flow. Therefore, a parametric study is performed to find the optimal design for placing piezoelectric polymers. The two-dimensional fluid structure-interaction analysis is performed based on the arbitrary Lagrangian–Eulerian scheme using COMSOL Multiphysics. Flow characteristics quantities, tip amplitude, and strain are evaluated at different arrangements of the SPs. The results reveal that wake control enhances effectively by doubling the number of SPs. The amplitude of the dual SPs increases by a remarkable ratio of 18.29 compared to the single plate. In the case of rigid and flexible SPs at a certain arrangement, dramatic reductions of 97.8% and 76.35% in the Strouhal number are obtained compared to a bare cylinder. In addition, 18% drag reduction compared to the bare cylinder is recorded for the rigid SPs. The presented passive method can be used as an attractive approach in flow control as well as energy harvesting from ocean waves and sea currents.

Keywords: cylinder; splitter plate; piezoelectric; fluid-solid interaction (FSI).

---

[*] Author to whom any correspondence should be addressed.

	Abbreviations	L	length of the SP [m]
ALE	arbitrary Laragia-Eulerian	P	gap between the SPs [m]
FFT	fast Fourier transform	p	fluid pressure [Pa]
FSI	fluid structure interaction	p_b	pressure at the rear stagnation point [Pa]
RMS	root mean square	p_∞	free stream pressure [Pa]
Re	Reynolds number	p_s	static pressure at the cylinder surface [Pa]
SP	splitter plate	t	time [s]
St	Strouhal number	u_f	fluid velocity [m/s]
VIV	vortex induced vibration	u_m	fluid velocity (moving coordinate) [m/s]
VS	vortex shedding	u^*_{rms}	non-dimensional RMS of streamwise velocity
	Nomenclature	U_∞	freestream velocity [m/s]
A	SPs tip amplitude [m]	v_s	velocity of SP [m/s]
C_D	drag coefficient	v^*_{rms}	non-dimensional RMS of traverse velocity
C_L	lift coefficient	W^*_Z	non-dimensional spanwise vorticity
C_P	pressure coefficient	X,Y	reference coordinates of the material frame
C_{Pb}	base pressure coefficient	x,y	spatial coordinates of the spatial frame
D	cylinder diameter [m]	S	gap between the cylinder and first SP [m]
F_D	drag force [N]		**Greek symbols**
F_L	lift force [N]	ε	strain
f_s	frequency of VS [Hz]	θ	angle
h	thickness of the SP [m]	μ	dynamic viscosity [Pa.s]
I	unit diagonal matrix	ρ	fluid density [kg/m^3]
		ρ_s	solid density [kg/m^3]

1. Introduction

The topic of fluid flow past a circular cylinder has been extensively studied in literature due to its importance in the industry [1]. Examples include submarines [2], wind industry [3], heat exchangers [4], automobiles [5], transmission lines [4], tall buildings [6], and bridges [5]. Vortex shedding (VS) is a well-known phenomenon that occurs on the back of a bluff body in the flow field [7, 8]. It causes oscillations in drag and lift forces on the structure and consequently induces vibration, which is known as vortex-induced vibration (VIV) [9]. The VIV may cause destructive effects on the structure such as fatigue failure, structural clashing, and lifetime reduction [10]. Hence, the reduction of VIV through wake modification has received prominent consideration in engineering within the past few decades [11-13]. The wake structure downstream of a cylinder can be modified using active or passive methods. In the active methods, external energy is used to weaken the flow wake, such as rotation [14, 15], blowing and suction [16-19], electromagnetic force [20], and synthetic jets [21-23]. In contrast, in the passive methods, improvement of the structure surface or adding additional parts is taken into account. Examples include slotted circular cylinder [24, 25], splitter plates (SPs) [26-29], shape modification [30, 31] and surface bumps [32-34]. The significant advantages of the passive strategies are their low costs of implementation and maintenance because they do not need additional energy [35]. Among passive methods, the implementation of SPs in the wake region of bluff bodies has been one of the most successful methods to suppress VS [36, 37]. It can effectively modify the key flow characteristics by inhibiting the interaction between the two shear layers that form in the wake region [38]. Using SPs can lead to wake stabilization, the extension of vortex formation length, elongation of vorticities, suppression of VS, reduction of hydrodynamic forces, and the Strouhal number [36, 39]. The influence of multiple rigid SPs with varying angles attached to the rear surface of a cylinder at Re=100 was studied by Abdi et al. [7]. The results revealed that two and three attached SPs were more effective than one SP in drag reduction. Furthermore, it was found that the attachment angle had a significant effect on the wake control and the maximum drag reduction occurred for two SPs case at an angle of 45°. Hwang et al. [40] examined the influence of two detached rigid SPs placed upstream and downstream of a cylinder on drag reduction. Their numerical study showed that the SP located upstream of the cylinder reduced the stagnation pressure and the SP located downstream of the cylinder increased the base pressure of the cylinder. The combination of both led to 38.6% reduction in the drag coefficient. Bao and Tao [41] investigated the influence of two rigid SPs attached symmetrically at the rear of cylinder. They found that the attachment angle influenced the wake control, and the maximum efficiency of suppression was achieved for the range of $40° \leq \theta_f \leq 50°$. Gerrard [27] investigated the influence of the length of a rigid SP on flow structure at Reynold number of 2×10^4. The results revealed that the best length to achieve the lowest Strouhal number (St) was equal to the cylinder diameter. In an experimental study by Roshko [28], it was demonstrated that when the ratio of the rigid SPs length to the cylinder diameter was equal to 5, the VS was completely suppressed. An attached hinged rigid SP was investigated by Shukla et al. [38]. It was observed the communication between the shear layers was not completely disrupted since the SP rotated about the hinged point. Other studies have investigated the effect of permeable and inclined SPs [42], an attached rigid wavy SP [43], and an upstream rod [44] on the flow structure around a cylinder.

Recently the application of flexible SPs has become popular for the flow control. Because in addition to high capability in control, it also can be used for energy harvesting from the flow. For instance, the SPs deformation due to VS can be utilized to harvest energy from the flow using piezoelectric polymers. These polymers are able to generate electric charges when they are under pressure or strain by converting mechanical energy into electrical energy [45]. Shukla et al. [46] have carried out experimental studies with a flexible SP and examined the influence of the SP’s flexural rigidity, length of SP, and Reynolds number on the flow characteristics of a cylinder. Results showed that that at high values of Reynolds number, two different oscillation regimes for the SP can be observed. The frequency of both regimes was close to the cylinder frequency. Moreover, it was found that the SPs that were considerably larger than the wake length had similar responses, whereas shorter SPs had significantly different responses. Wu et al. [47] numerically studied a detached flexible SP, which was placed at the downstream or upstream of a fixed cylinder using the immersed boundary-Lattice Boltzmann method. The SP was under a forced oscillation and was deformed in a fish-like movement at Re=100. The results indicated that the flexible downstream SP has more effect on drag reduction compared to the rigid one due to the fish-like motion of the SP. In addition, a further drag reduction was achieved using upstream flexible SP compared to downstream one. Sun et al. [48] investigated flow-induced-vibration of aflexible SP attached to a cylinder at Re=100. It was observed that the cylinder with the SP has less drag, but a higher oscillation amplitude compared to a bare cylinder. Chehreh and Javadi [49] numerically studied the effect of two SPs that were attached at specific angles (±55 degrees) behind a cylinder at Re=100 and 200. The SPs were under forced oscillation at various ratios of the natural VS frequencies. Results showed that by increasing the frequency ratio and the oscillation amplitude, an in-phase VS pattern in the wake structure was observed resulting in complete VS suppression. In another work, Abdi et al. [8] studied the effect of adding single and multiple attached flexible SPs downstream of a cylinder at Re=100 using Arbitrary Lagrangian–Eulerian (ALE) scheme. They evaluated the effect of SP flexibility and attachment angle on drag, lift, and the Strouhal number. Results showed that in contrast to rigid cases, a slight increase in the Strouhal number (St) was observed in flexible cases. The increase in St originated from formation of a tiny vortex in the tip of SP, which was called tip vortex. Pfister and Marquet [50] numerically studied the dynamics of a hyperplastic attached SP subjected to a laminar flow at Re=80. Numerical approach was based on the ALE formulation of the incompressible Navier–Stokes equations (flow modeling), coupled with a Saint-Venant Kirchhoff model (SP modeling).

As discussed above, several studies have focused on the rigid SPs. Some others focused on the attached flexible SPs. The usage of detached SPs and the possible advantages of using several SPs should be studied further. In addition, electricity generation from flexible SPs by piezoelectric polymers requires more information related to the SPs' strain. To this aim, a comparative study is done on a circular cylinder with both rigid and flexible SPs. One and two detached SPs are considered downstream of a circular cylinder. The distance between the first SP and cylinder as well as between the SPs are varied. For flexible SPs, the tip amplitude and strain were measured to harvest energy from the flow. The optimum arrangements of the SPs for placing piezoelectric polymers in terms of both flow control and electricity generation are obtained. This study focuses only on Re=100 in a two-dimensional FSI problem to avoid the three-dimensional flow nature that occurs at Re > 160 [49]. Considering the current worldwide energy demands, and transition into clean energy, the use of such flexible SPs provides significant benefits over the conventional cylindrical structure which include benefit of energy harvesting along with reducing structural fatigue failure and increasing the lifetime.

The remainder of this paper is structured in four sections. The numerical methodology and validation of the simulation model are described in section 2. The results that include amplitude and strain of the SPs during fluctuation and flow characteristic variables are provided in section 3. Eventually, the summary and conclusions are discussed in section 4.

2. Materials and methods

2.1. Problem statement

As illustrated in Fig. 1(a), in this study a circular cylinder with one and two detached rigid SPs was modeled. A similar geometry with flexible SPs was modeled as well (Fig. 1(b)). The SPs are located downstream of the cylinder in a horizontal line crossing center of the cylinder. The ratio of the gap between the cylinder and the first SP (S), to the cylinder diameter (D) varies in the range of $0 \leq S/D \leq 2.5$, and the ratio of the gap between the SPs (P) to the cylinder diameter (D) is in the range of $0 \leq P/D \leq 3$. It should be noted that the first SP can be attached to the cylinder as well. The lengths of the SPs are the same and equal to the cylinder diameter (L/D=1) to minimize the Strouhal number [27]. The thickness (h) of the SPs is set at 0.03D. The computational domain size and the related boundary conditions are displayed in Fig. 2. The dimension of the computational fluid domain is 80D×60D [8]. The distance between the inlet to the center of the cylinder is 20D. The upper and lower boundaries are located at 30D from the cylinder's center. Hence, the dimension of the computational domain is sufficiently large, so that the effect of the blockage ratio is negligible. No-slip boundary condition is applied to the surface of the cylinder and SPs. Therefore, the fluid velocity (u_f) on the cylinder is equal to zero, and on the flexible SPs $u_f = v_s$ (v_s is the SP velocity).

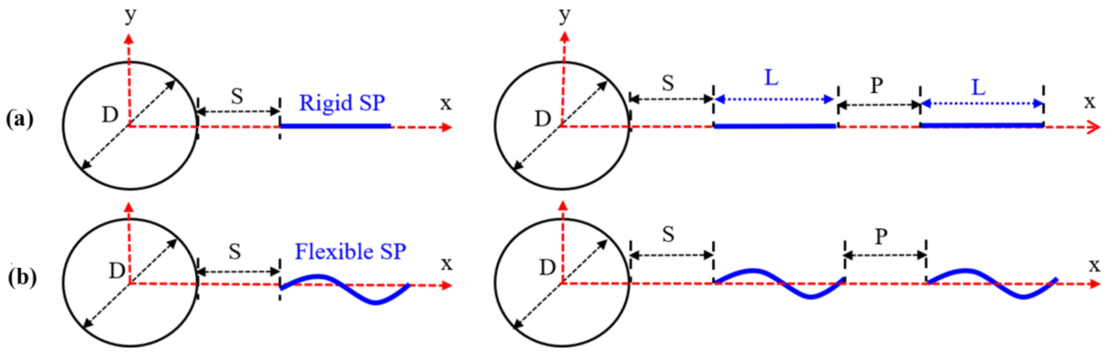

FIG. 1. Configuration of the cylinder with one and two SPs: (a) rigid, (b) flexible.

The fluid flow enters the computational domain from the inlet boundary with a velocity of U_∞ and exits from the outlet boundary with zero gradient pressure. The open boundary condition with no viscous stress is applied to the upper and lower boundaries. The cylinder and the front edge (left side) of the detached flexible SPs are fixed. Table 1 presents the material properties for fluid and solid domains. The choice of material for this study is based on several requirements. The flow must be able to deform the SPs and the typical fluid candidate for such a numerical study is glycerin which has a relatively high viscosity [51]. For solid domain, the stiffness of SPs must be low enough to oscillate at reasonable amplitude. For this reason, the SPs are made of cork which has a high elasticity.

Table 1. Material properties used in the computational domain.

	Material	Density	Poisson's ratio	Young's modulus	Dynamic viscosity
Fluid domain	Glycerin	1260 kg/m^3	-	-	1.42 $Pa.s$
Solid domain	Cork	180 kg/m^3	0.3	32 MPa	-

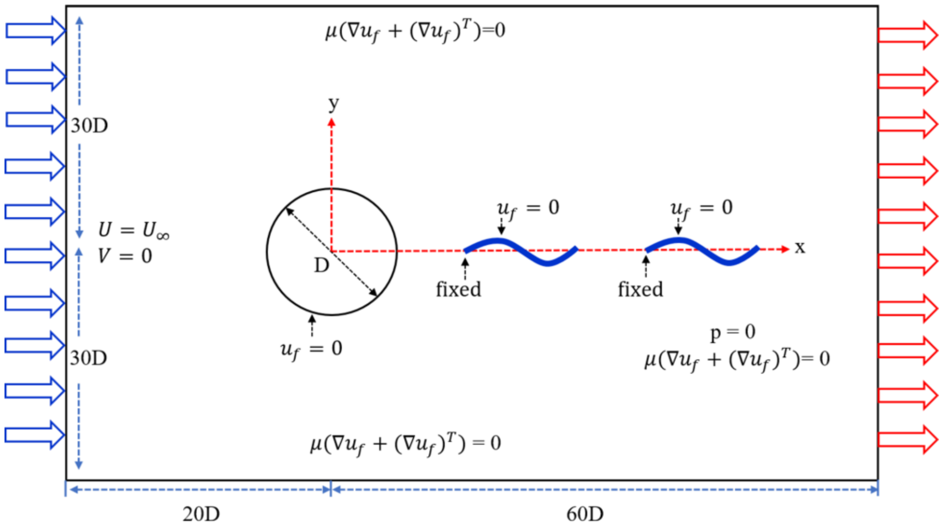

FIG. 2. The computational domain and boundary conditions.

2.2. Governing equations

The numerical procedure is based on the finite element method using the COMSOL Multiphysics software (version 5.4, COMSOL Inc., Burlington, MA). The Arbitrary

Lagrangian-Eulerian (ALE) scheme is used to simulate this fluid-structure interaction problem with a fully coupled approach. In the ALE scheme, the equations of the fluid domain are formulated based on the Eulerian description at a spatial frame, and the deformation equations of the solid material are formulated based on the Lagrangian description at a material (reference) frame. Due to the flexibility of the grid in the ALE method, it is beneficial in problems with large deformations [52]. The governing equations of fluid flow, solid mechanics, coupling interface, and moving mesh are described in the following sections.

2.2.1. Fluid dynamics

The fluid flow is considered to be incompressible and Newtonian. The Navier-Stokes equations in the spatial coordinate system are as follows [53]:

$$\nabla . u_f = 0 \tag{1}$$

$$\rho \frac{\partial u_f}{\partial t} - \nabla . \left[-pI + \mu(\nabla u_f + (\nabla u_f)^T) \right] + \rho(u_f - u_m) . \nabla u_f = 0 \tag{2}$$

where $(\bullet)^T$ represents a transpose, I denotes the unit diagonal matrix, p is the pressure, μ is the dynamic viscosity, ρ is the density of the fluid, u_m is the fluid velocity corresponding to a moving coordinate system, and t is time. The initial conditions for the fluid domain are:

$$p = 0 \text{ and } u_f = 0 \tag{3}$$

Furthermore, a force transformation is required due to the adoption of different coordinate systems in the ALE method [8]:

$$F = f . \left(\frac{dv}{dV} \right) \tag{4}$$

Here, f and F denote the force in the spatial and the material frames, respectively, and dv and dV are the scale factors for the spatial frame and the material frame, respectively.

2.2.2. Solid mechanics

Numerical formulation of the SPs in the material frame (undeformed) coordinate system is as follows:

$$(S - S_0) = C : (\varepsilon - \varepsilon_0) \tag{5}$$

Here, S is the second Piola–Kirchhoff stress tensor and C is the fourth-order elasticity tensor, ε is the Green–Lagrange strain, ‘‘:’’ is the double-dot tensor product (double contraction), S_0 and ε_0 stand for the initial quantities. In the above equation, ε is given by:

$$\varepsilon = 0.5 \left[(\nabla u_s)^T + \nabla u_s + (\nabla u_s)^T \nabla u_s \right] \tag{6}$$

where u_s is the displacement vector. Based on linear elastic assumption, the deformation of SP is calculated by:

$$\rho_s \frac{\partial^2 u_s}{\partial t^2} - \nabla . \sigma = F_V \tag{7}$$

where ρ_s is density of solid domain, F_V is the force per unit volume at the SPs surface, and σ is the Cauchy stress. The initial conditions for the solid domain are adjusted as:

$$u_s = 0 \text{ and } \frac{\partial u_s}{\partial t} = 0 \tag{8}$$

2.2.3. Coupling and interface consideration

In the coupling process of the fluid domain with the solid one, it is essential to satisfy the boundary conditions related to the contact interface. The u_f is obtained from the flexible SPs velocity (v_s) at the interface:

$$u_f = v_s \tag{9}$$

The stress on the SPs at the interface of the two domains is computed from the following equation:

$$\Gamma . n^f + \sigma . n^s = 0 \tag{10}$$

where Γ and σ are the stress tensors and n^f and n^s are the normal vectors of the fluid and SPs, respectively. The Γ is the sum of pressure and viscous stresses of the fluid:

$$\Gamma = -pI + \mu(\nabla u_f + (\nabla u_f)^T) \tag{11}$$

2.2.4. Moving mesh

The computational mesh deforms to adjust to the deformation of the flexible SPs. In the moving mesh interface, the Winslow smoothing equations are applied [54].

$$\frac{\partial^2 \partial X}{\partial x^2 \partial t} + \frac{\partial^2 \partial X}{\partial y^2 \partial t} = 0 \tag{12}$$

$$\frac{\partial^2 \partial Y}{\partial x^2 \partial t} + \frac{\partial^2 \partial Y}{\partial y^2 \partial t} = 0 \tag{13}$$

where, X and Y denote the reference coordinates of the material frame (solid domain), and x and y are related to the spatial coordinates of the spatial frame (fluid domain) [8].

2.3. Non-dimensional flow parameters

It is a common approach to describe physical phenomena in non-dimensional forms in order to achieved generalized results comparable with other studies. Accordingly, important non-dimensional parameters associated with flow characteristics are defined by equations (14) to (23):

2.3.1. Strouhal number

The frequency of VS is characterized by a dimensionless parameter known as the Strouhal number (St), which is defined as follow:

$$St = \frac{f_s D}{U_\infty} \tag{14}$$

where f_s is the frequency of VS, D is the cylinder diameter and U_∞ is the free stream velocity of flow.

2.3.2. Hydrodynamic coefficients

The most frequently used flow quantities in an unsteady flow regime are lift coefficient (C_l) and drag coefficient (C_d), which are defined by:

$$C_l = \frac{F_l}{0.5\rho U_\infty^2 D} \tag{15}$$

$$C_d = \frac{F_d}{0.5\rho U_\infty^2 D} \tag{16}$$

Here, F_l and F_d are lift and drag forces, which are the force components that are applied to the bluff body perpendicular and parallel to the flow direction, respectively.

2.3.3. Pressure coefficients

The drag force is a combination of pressure and viscous forces applied to the surface by the fluid. Meanwhile, the pressure force is the dominant part of the drag, which is highly dependent on shape of bluff bodies. Due to the importance of pressure drag, the pressure coefficient is introduced, which describes the pressure difference between reference pressure and surface pressure as follows:

$$C_P = \frac{p_s - p_\infty}{0.5\rho U_\infty^2} \tag{17}$$

where p_s is the static pressure on the cylinder surface, p_∞ is the free-stream static pressure far from the bluff body and $0.5\rho U_\infty^2$ is the dynamic pressure. If the pressure of the rear stagnation point (p_b) is used in equation (17), the base pressure coefficient (C_{Pb}) can be obtained [55, 56]:

$$C_{Pb} = \frac{p_b - p_\infty}{0.5\rho U_\infty^2} \tag{18}$$

2.3.4. Root-mean-square (RMS) of velocity

In the wake region of a bluff body, the root-mean square of streamwise velocity (u_{rms}) and transverse velocity (v_{rms}) show the roll-up position of shear layers and the interaction between them, which are defined by:

$$u_{rms} = \sqrt{\frac{1}{N}\sum_{i=1}^{N}(u_i - \bar{u})^2} \tag{19}$$

$$v_{rms} = \sqrt{\frac{1}{N}\sum_{i=1}^{N}(v_i - \bar{v})^2} \tag{20}$$

In these relations, $\bar{u}$ and $\bar{v}$ are the time averaged of streamwise and transverse velocities, N is the number of samples in the time history, and u_i and v_i denote the temporal series. The dimensionless forms of them are as follow:

$$u_{rms}^{*} = \frac{u_{rms}}{U_\infty} \tag{21}$$

$$v_{rms}^{*} = \frac{v_{rms}}{U_\infty} \tag{22}$$

2.3.5. Spanwise vorticity

Vorticity is rotation of the fluid particles around a fixed axis. It can represent the boundary layer, the shear layer growth, and VS phenomena. The dimensionless spanwise vorticity (W_Z^*) is given by [57]:

$$W_Z^* = \left(\frac{\partial v}{\partial x} - \frac{\partial u}{\partial y}\right)\frac{D}{U_\infty} \tag{23}$$

2.4. Mesh description

As displayed in Fig. 3 (a), an unstructured mesh is employed for the computational domain due to the high adaptability of the triangular elements with the fluid domain. The circumferences of the cylinder and SPs are discretized by extremely fine cells. For accurate estimation of velocity and pressure gradients, two layers of structural cells are utilized for the SPs and cylinder surfaces (Fig. 3(b)). Table 2 demonstrates the dependence of the Strouhal number and time average of the drag coefficient ($\overline{C_d}$) on the mesh resolution for the cylinder with two SPs ($S = P = 0.5D$). According to the results, the setting of case “c” is selected.

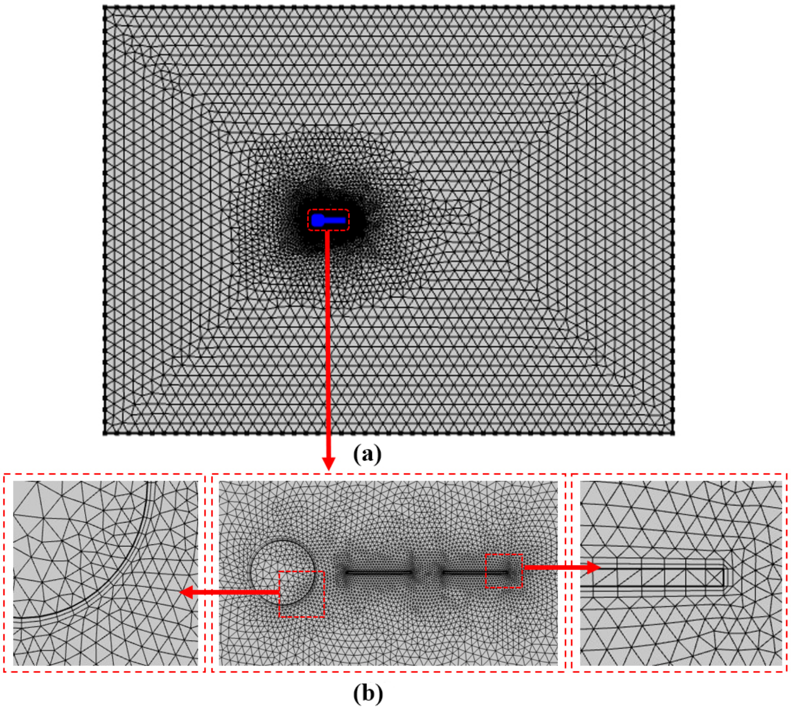
(a)

(b)

FIG. 3. Meshing of the computational domain, (a) view of the whole domain, (b) zoomed view of the mesh around the cylinder and SP.

Table 2. Grid independence study for a fixed cylinder with two detached flexible SPs ($S = P = 0.5D$).

Case	Number of elements	St	$\overline{C_d}$
a	8001	0.157	1.152
b	10673	0.158	1.153
c	15556	0.159	1.157
d	30830	0.159	1.158

2.5. Validation of the model

The model is validated by the numerical and experimental results of flow past a circular cylinder as well as flow past a cylinder with one attached rigid SP at Re=100 in the literature. As can be seen in Table 3, the results of St, $\overline{C_d}$, and RMS of the lift coefficient ($C_{l_{rms}}$) are in good agreement with the corresponding results of other studies. Furthermore, the results of one attached flexible SP case are compared with the numerical results of Turek and Hron [51] in Table 4. In this case, Re=200 and the length and thickness of the SP are 0.35 m and 0.02 m, respectively. Both frequency and magnitude of F_L and F_D on the cylinder and SP are compared in Table 4. The results again show a good agreement with the corresponding ones.

Table 3. Validation of the results of a cylinder with and without attached rigid SP at Re=100.

Test case	Bare cylinder (Re=100)			One attached rigid SP (Re=100, L/D=1)	
Flow quantity	St	$\overline{C_d}$	$C_{l_{rms}}$	St	$\overline{C_d}$
Sudhakar and Vengadesan [4]	0.165	1.37	-	0.139	1.174
Norberg [58]	0.164	-	0.22	-	-
Williamson [59]	0.164	-	-	-	-
Hwang and Yang [40]	0.167	1.34	-	0.137	1.17
Present study	0.164	1.33	0.228	0.136	1.161

Table 4. Validation of the results of a cylinder with one flexible SP at Re=200.

Test case	Drag force		Lift force	
	Magnitude (N)	Frequency (Hz)	Magnitude (N)	Frequency (Hz)
Turek and Hron [51]	149.78±2.22	10.9	457.3±22.66	5.3
Present study	150±4.49	10.43	454±24.78	5.33

3. Results and discussion

In this section, flow characteristics including contours of vorticity, streamlines, velocities, and values of St, $\overline{C_d}$, $\overline{C_P}$, $\overline{C_{Pb}}$ and Cl_{rms} at different arrangement of SPs are studied. The results are evaluated as a function of S/D and P/D.

3.1. Contours of vorticity and streamlines

Figure 4(a) demonstrates an example of instantaneous dimensionless spanwise vorticity contours (W_z^*) for a half cycle of SPs oscillation in the case of two flexible SPs ($S/D = 2.5$ and $P/D = 1.5$). The x and y coordinates become dimensionless with the cylinder diameter (D). The beginning of the cycle (0T) is attributed to the highest displacement of the first SP. Two shear layers consisting of positive vorticity (counterclockwise) and negative vorticity (clockwise) can be observed in the vorticity contours [60]. These shear layers roll up simultaneously with the SPs flapping movement. Under the shedding mechanism, the first SP (the SP close to the cylinder) interacts with shear layers of the cylinder. Then, the second SP experiences the shear layers affected by the first SP. The movement of the SPs has a phase difference of 180° and they deform in the opposite directions to each other. When the first SP is at the maximum displacement in the +y direction, the second SP is at the maximum displacement in the -y direction. In addition to the main shear layers of the cylinder, small shear layers extend over and below of the SPs. The small shear layers slip at the SPs surfaces and roll up at the tip of the plate. The interaction between the main shear layers of the cylinder and the small shear layers at the tip of SPs results in two different mechanisms which will be called here after destructive mechanism and constructive mechanism. When the shear layers (from the cylinder and from the SPs) have the same sign, vorticities merge with each other and produce a shear layer with higher strength and if they have opposite sign, they weaken each other. It can be seen that the shear layers of the first and the second SPs have destructive and constructive mechanisms, respectively. The displacement of the first SP is more than the second SP. Because the cylinder shear layers that interact with the first SP are strong and after contacting with the first SPs shear layer, they become weak. Figure 4(b) indicates the corresponding contour for the case of rigid SPs. Similar to the flexible case, the shear layers of the first and the second SPs have destructive and constructive mechanisms, respectively. However, in the second SP of the rigid case, a new destructive mechanism appears at the fixed edge of the SP. In both rigid and flexible cases, the SPs prevent the main shear layers to interact with each other. Consequently, they expand and interact with each other after the second SP. In this arrangement of SPs, the elongation of vortices along two flexible and rigid SPs leads to 15% and 29.55% reduction in the St compared to the bare cylinder, respectively. The reason for the higher wake suppression in the case of rigid SPs compared to the flexible ones in this arrangement of SPs is attributed to the flexibility of the SPs which is discussed in the following paragraph.

The streamlines pattern is provided for a half cycle of SPs oscillation in Fig. 5 for flexible SPs at $S/D = 2.5$ and $P/D = 1.5$. The corresponding results of the rigid SPs are depicted on the right column of Fig. 5. The better performance of rigid SPs in St reduction compared to the flexible ones could be justified using three mechanisms that can be seen in streamlines. Firstly, the downward motion of the first flexible SP gives more space to the upper vortex near the cylinder to grow. Therefore, it grows faster than the corresponding vortex of the rigid SPs. Secondly, on the other side of the first SP, the lower vortex at the same period is bigger in the case of flexible SPs compared to the rigid ones. The third mechanism is related to the generation of a tiny vortex near the tip of the first SP (here after called “tip vortex”) in both rigid and flexible cases. This tip vortex develop more instability in the wake structure. As can be seen in Fig. 5(a) for flexible case, the “tip vortex” generates at the tip of the first SP in a time cycle of 0.1T, and then separates at 0.2T. However, in the rigid case, it forms between the time cycles of 0T and 0.1T and eventually, it is completely separated from the first SP at 0.1T. In both cases, the separated tip vortices joins the converging streamlines. These observations confirm the better performance of rigid SPs compared to the corresponding flexible ones in terms of St reduction.

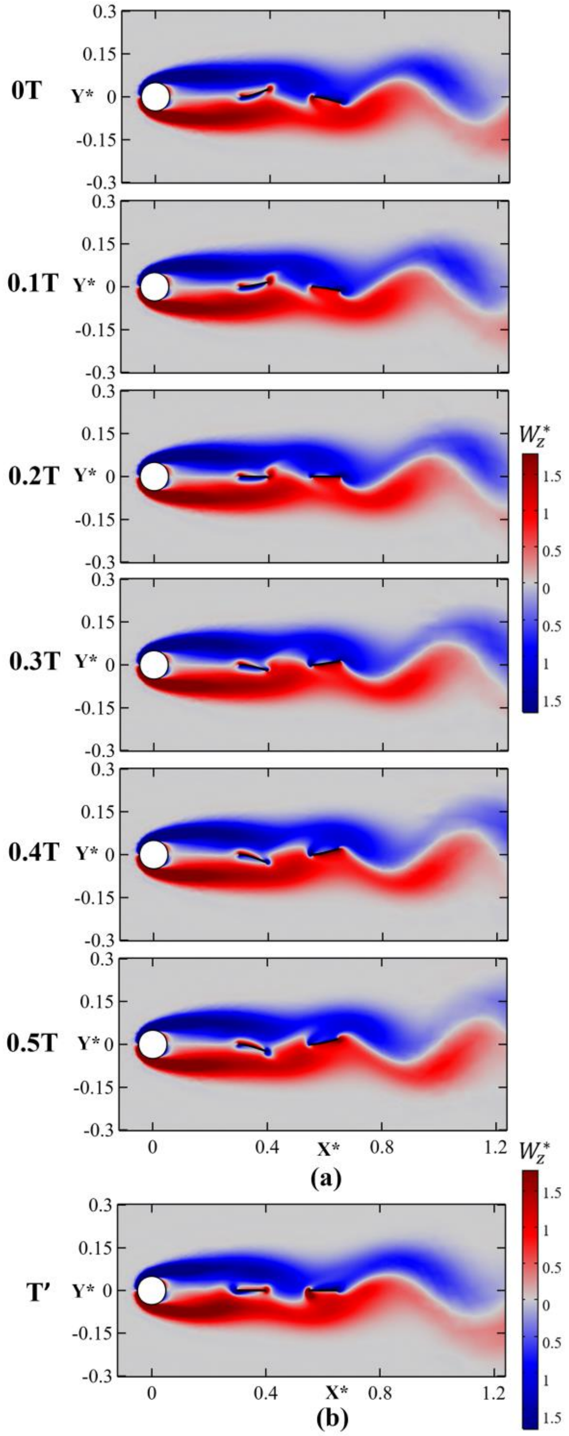

FIG. 4. Instantaneous dimensionless spanwise vorticity contours (W_Z^*) for two detached SPs at ($S/D = 2.5$ and $P/D = 1.5$): (a) flexible SPs during a half cycle of SPs oscillation, (b) rigid SPs.

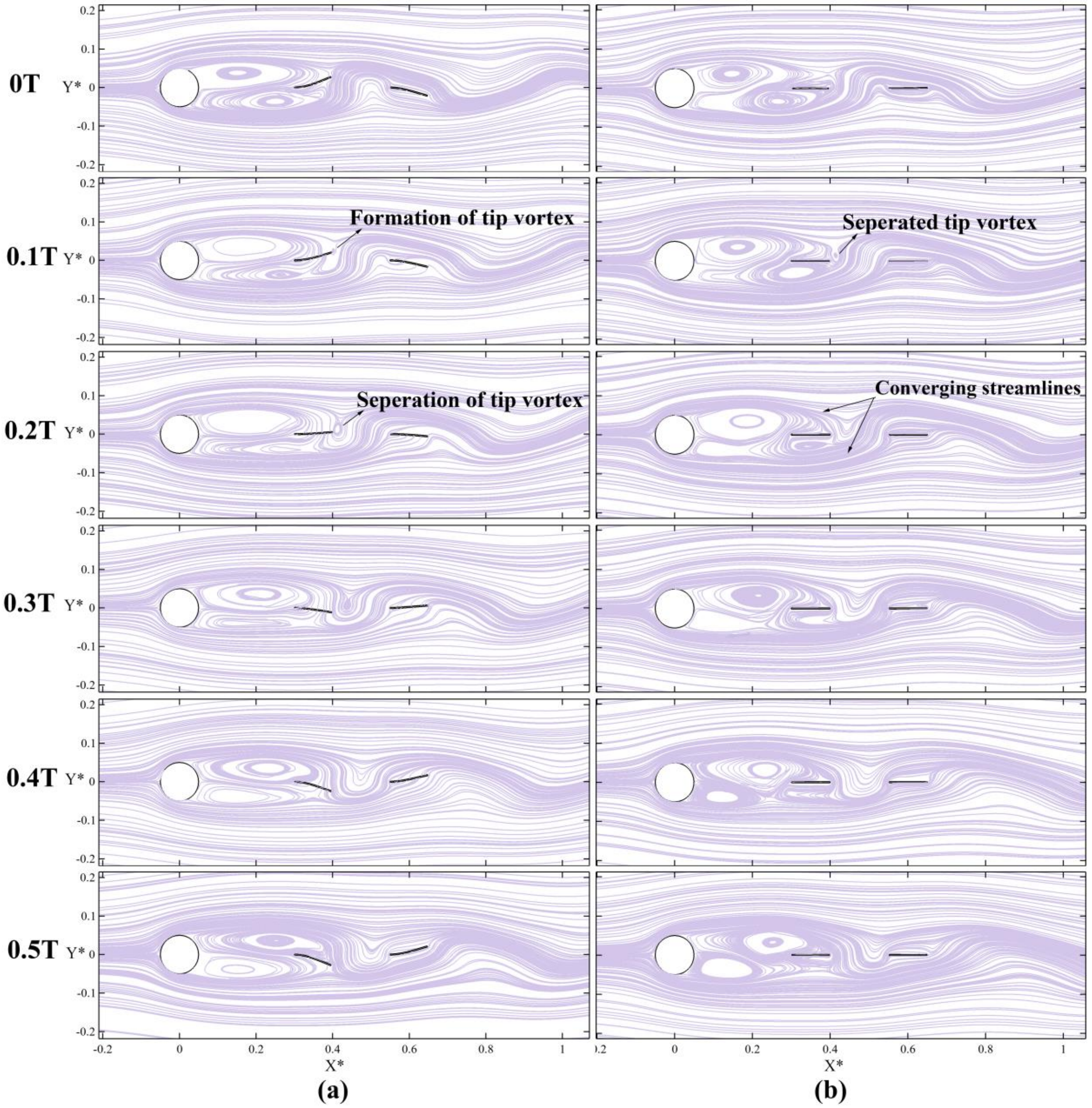

FIG. 5. Streamline patterns for a half cycle of oscillation in the case of two SPs ($S/D = 2.5$ and $P/D = 1.5$): (a) flexible SPs (b) rigid SPs.

3.2. Strouhal number

In this section, the Strouhal number is evaluated at different arrangements of the SPs. The St represents VS phenomenon and is calculated from FFT (Fast Fourier Transform) algorithm over the time history of the lift force. The variation of St against S/D for the cases of flexible SPs is demonstrated in Fig. 6(a). The corresponding results for the cases of rigid SPs are presented in Fig. 6(b). In addition, the result of the bare cylinder case is included in both plots. Using the rigid and flexible SPs as a passive control method reduces the St compared to the bare cylinder except some specific arrangements of flexible SPs (one SP at $S/D \leq 0.5$ as well as two SPs at $S/D = 0$ and $2 \leq P/D \leq 3$) in which a slight enhancement in St is observed. Maximum enhancement of St among these cases occurs in one attached SP case ($S/D = 0$) with 8.0% increase compared to bare cylinder. It is in agreement with the numerical study of Abdi et al. [8]. The increase in St is due to the formation of a “tip vortex” in the first SP. It interacts with the main vortices shedding from the cylinder and causes an increase in instability in the shear layers of the cylinder. As shown in Fig. 6(a), the Strouhal number of two flexible cases monotonically decreases for $P/D \geq 0.5$ as S/D increases (except the case with $S/D = 0.5$, $P/D = 3$). There are three local minimum in the St graphs: In one SP at $S/D = 1$ and in two SPs when $S/D = 0.5$ and $P/D = 3$ as well as at $S/D = 1.5$ and $S/D = 2$ in $P/D = 0$.The reason for these sudden drop will be discussed later ~~in~~ below Fig. 7. As shown in Fig. 6(b), the St in all cases with rigid SPs decreases compared to bare cylinder. The VS from the cylinder is very sensitive to arrangements of the SPs. Similar to flexible cases, there are some sudden reductions at $S/D = 1.5$ and $S/D = 2$. These sudden reductions are due to significant modifications in the flow patterns in which the VS is suppressed perfectly. As the distance between the rigid SPs increase to $P/D \geq 2$, the effect of SPs on wake structure becomes less and the St number increases. The rigid SPs at a close distance to each other act like a long SP and interrupt the contact between the shear layers of the cylinder. The most noticeable St reduction in both cases of rigid and flexible SPs occurs in the case of two SPs with the gap ratio of $S/D = 1.5$ and $P/D = 0$. This configuration results in a dramatic reduction of 97.8% and 76.35% in St compared to the bare cylinder in the case of rigid and flexible SPs, respectively. In addition, compared to the attached cases ($S/D = 0$ and $P/D = 0$), the corresponding configuration of $S/D = 1.5$ and $P/D = 0$ reduce the St by 97.2% and 71.2% in the case of rigid and flexible SPs, respectively. It indicates that the wake control can enhances effectively using detached SPs instead of attached ones.

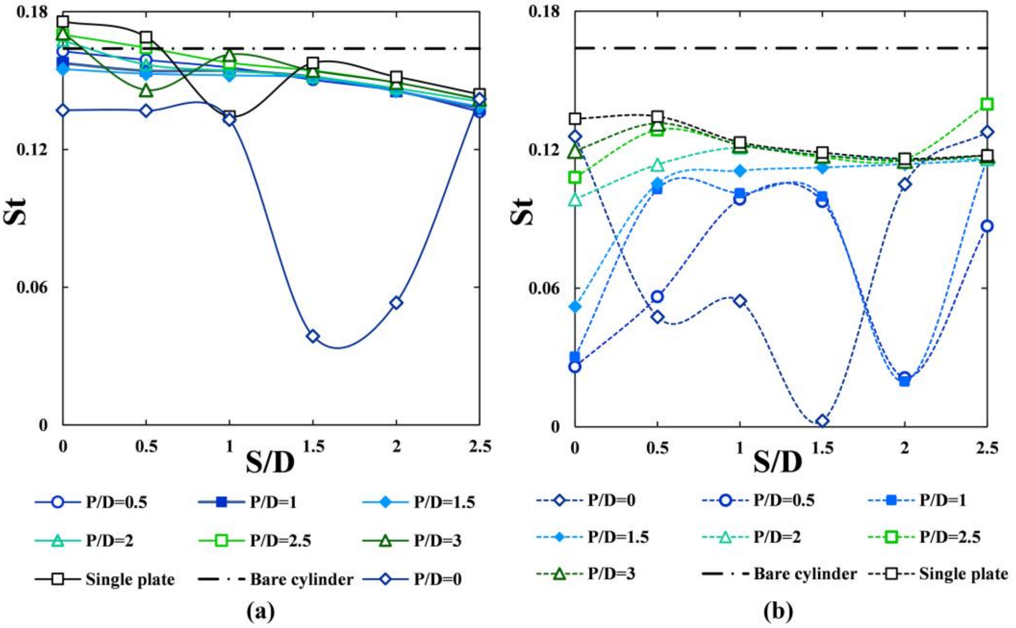

(a) (b)

FIG. 6. Strouhal number at various P/D and S/D: (a) flexible SPs, (b) rigid SPs.

To further explore the underlying mechanisms of the sudden St reductions in the cases of two flexible SPs at $P/D = 0$ & 3 and one flexible SP at $S/D = 1$, the streamlines at different S/D are presented in Fig. 7. As shown in Fig. 7(a), as S/D increases in the case of two flexible SPs at $P/D = 3$, two strong cylinder vortices expand further from the cylinder, and consequently the St number decreases. In contrast to other cases, at $S/D = 0.5$ in Fig. 7(a), it is observed that the expanded cylinder vortices divided into four vortices in the wake region. The two stronger ones are transferred downstream with the fluid flow and two smaller vortices near the cylinder grow and expand to repeat the same cycle. Similar to Fig.7(a), vortices elongate by increasing the S/D in Fig. 7(b). There is a distinct flow pattern for one SP case at $S/D = 1$ in which the shear layers cannot interact with each other properly. As can be seen in Fig. 7(c), the vortices are elongated more compared to Fig. 7(a) and Fig. 7(b) and they reach to their maximum length at $S/D = 1.5$ and 2 corresponding to their lowest St number. From these observations, it is expected that significant reduction occurs in drag and lift forces in the unsteady flow (as can be seen in Fig. 10(a) and Fig. 13). These effective control performances are achieved using detached SPs, which has a noticeable effect on the wake stabilization. It is interesting to note that these two flexible SPs cases, do not have any oscillations in the mentioned arrangements and only low amplitude oscillation exist in the one SP case at $S/D = 1$ (Fig. 16).

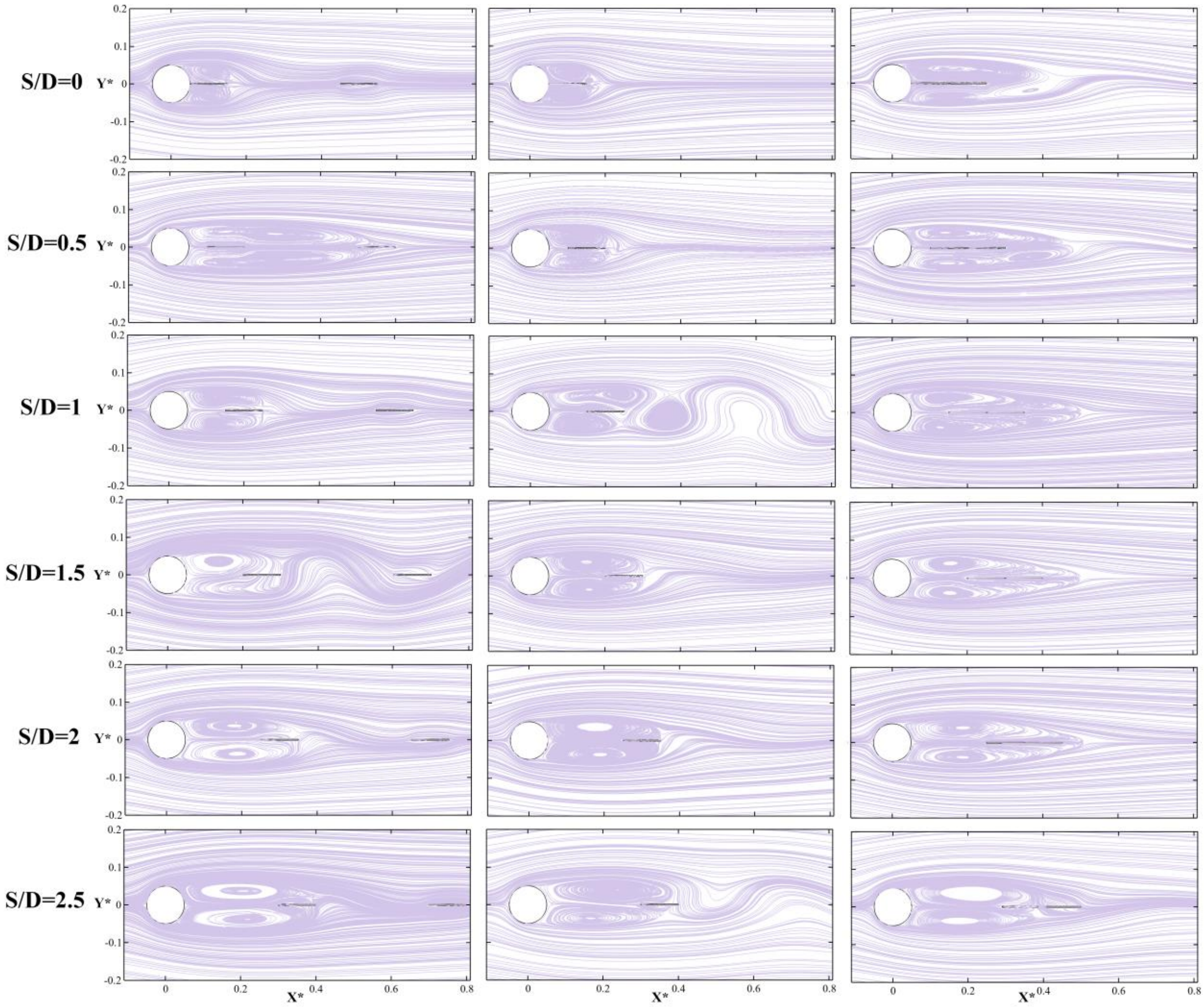

(a) (b) (c)

FIG. 7. Time-averaged streamlines for flexible SPs at different S/D: (a) two SPs case ($P/D = 3$), (b) one SP case, (c) two SPs case ($P/D = 0$).

To investigate the dynamics of the mean wake flow for the case of flexible and rigid SPs, contours of dimensionless RMS of streamwise velocity (u^*_{rms}) and transverse velocity (v^*_{rms}) at different P/D and fixed $S/D = 2$ are displayed in Fig. 8 and Fig. 9, respectively. In von-Karman Street, the vorticity diffusion mechanism is affected by the fluctuations in velocity. Hence, the reduction of velocity fluctuations can be a representative of elimination of the VS. Using the SPs in this study leads to a reduction in velocity fluctuations and consequently suppression of the VS. Depending on the position of the SPs, there are two or four peaks in the profile of u^*_{rms} (Fig. 8). The peaks coincide with the roll-up locations of the shear layers and are distributed symmetrically with respect to the centerline of the cylinder [55]. For flexible SPs at $P/D = 0.5$, the velocity fluctuations between the two SPs are very small, so only two peaks can be observed after the second SP. By increasing the distance between SPs ($P/D \geq 1$), more space is available for rolling up the shear layers in the wake structure. As can be seen in Fig. 8 for $P/D \geq 1$, two peaks are generated between the SPs and gradually becomes stronger. A similar trend can be seen for the rigid cases. However, the peaks between the SPs as well as after the second SP are generated at $P/D \geq 1.5$. The distribution of v_{rms} can be attributed to the variation of the lift force [61]. So, it can be utilized as a representative of the lift variation to evaluate the effectiveness of the proposed control method. Moreover, v_{rms} indicates the interaction between the wake vortices. The value of v^*_{rms} for all cases decreases significantly compared to the bare cylinder. As can be seen in Fig. 9 (a) , the peak location alters by changing P/D. For the flexible cases, it forms between the two SPs at $P/D = 0.5$, and it increases gradually in both size and value of the v^*_{rms}. the second plate moves further away, there is more free space for the interaction of the shear layers and consequently, the velocity fluctuation increases. There are two main regions for formation of the large peaks: the frontal edge of the second SP, where the sharp edges facilitate growth of the shear layers, and downstream area of the second SP, where the vortices can form freely. For the rigid cases (Fig. 9 (b)), there is no peak at $P/D \leq 1$. By increasing P/D, in contrast to other cases, four peaks are captured in the wake region at $P/D = 1.5$ and $P/D = 2$. Two peaks are formed between the SPs in the vicinity of the SPs edges. Also, two peaks are apparent after the second SP, which tend to be asymmetric relative to the wake centerline. By further increase of P/D ($P/D \geq 2.5$), the distribution of v^*_{rms} becomes symmetric with respect to the wake centerline. Moreover, one strong peak is formed on the front edge of the second SP. For the rigid SPs, the maximum value of v^*_{rms} occurs on the front edge of the second SP at $P/D = 2$ due to strong curling of the shear layers besides the constructive mechanism of interactions of shear layers of the cylinder and SP. As can be seen in Fig. 8 and Fig. 9, the velocity fluctuations for specific arrangement of the flexible case ($P/D = 0$) and the rigid case ($0 \leq P/D \leq 1$), are almost zero and no peak is captured. The reason is that the short distance between the two SPs (P/D), causes the SPs to behave like a continuous long SP. Hence, the SPs prevent the contact between shear layers and the symmetric vortices form along the SPs. Consequently, the velocity fluctuations are negligible.

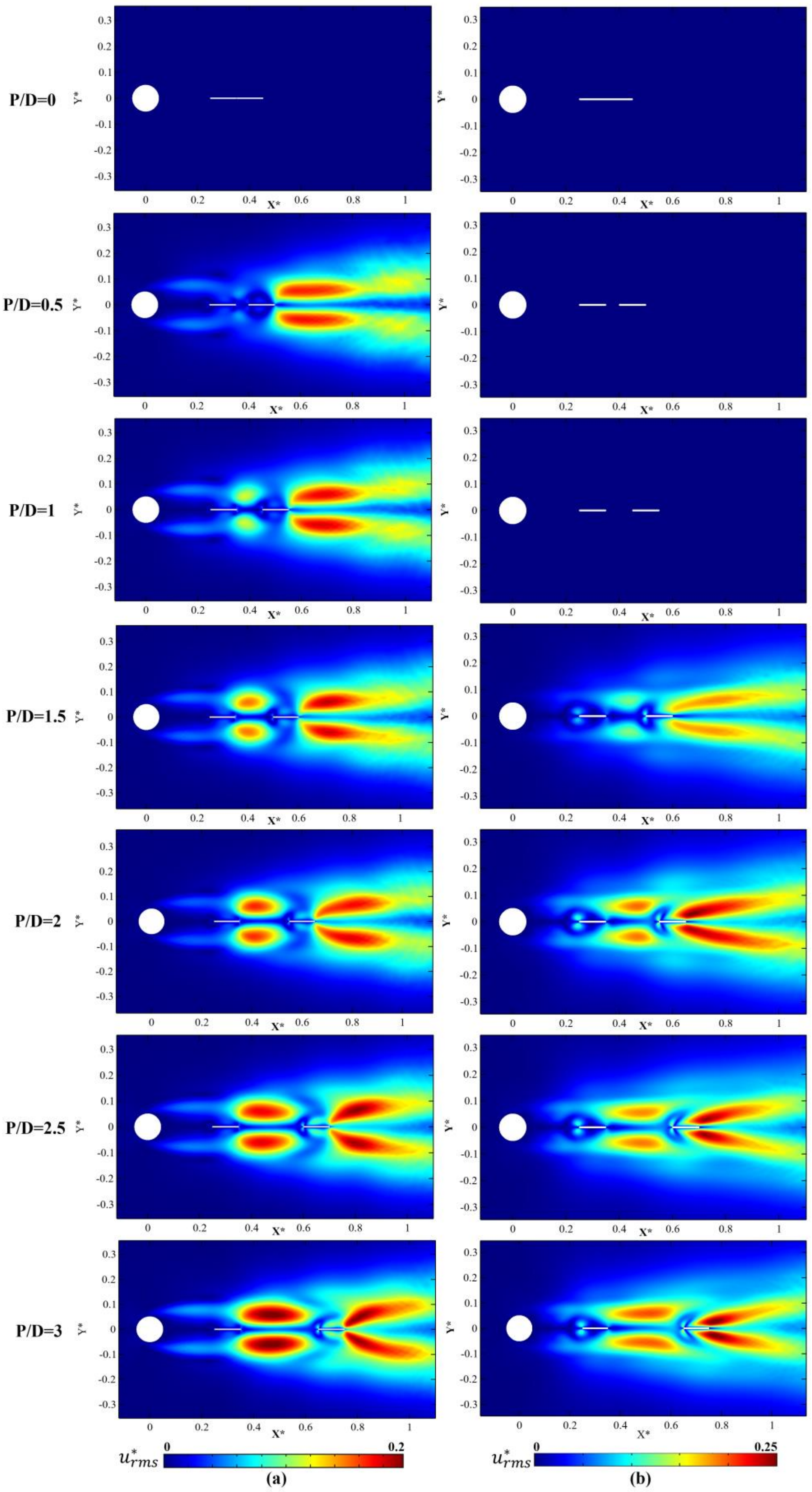

FIG. 8. Contours of dimensionless RMS of the streamwise velocities (u^*) against P/D at S/D =2: (a) flexible cases, (b) rigid cases.

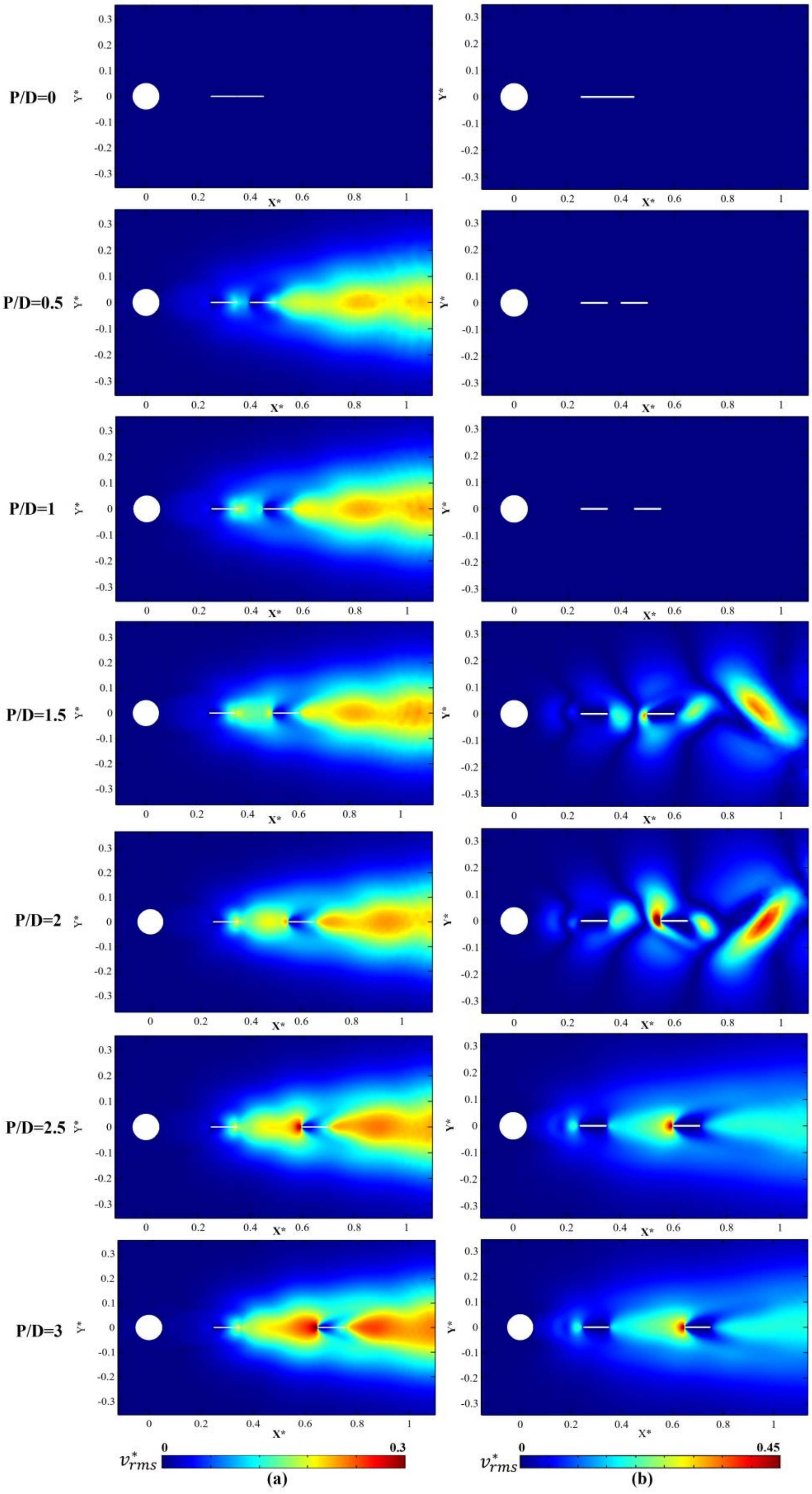

FIG. 9. Contours of dimensionless RMS of the transverse velocities (v^*) at different P/D and fixed S/D =2: (a) flexible cases, (b) rigid cases.

3.3. Hydrodynamic coefficients

Hydrodynamic forces are evaluated in this section to assess the effect of the SPs in the suppression of VS. Oscillations in drag and lift forces resulted in vibration of the structure, which has a destructive impact on lifetime. The drag coefficient is calculated in two ways in this study; forces are integrated over the cylinder surface ($\overline{C_d}$), or they are integrated over the cylinder and SPs surfaces ($\overline{C_{dt}}$). Fig. 10(a)-(b) display the $\overline{C_d}$ versus S/D for flexible and rigid SPs and the corresponding results of $\overline{C_{dt}}$ are depicted in Fig. 10(c)-(d), respectively. Fig. 10(a)-(b) clearly shows significant reductions in the mean drag coefficients compared to the bare cylinder. For the flexible case (Fig. 10(a)), the overall trend of $\overline{C_d}$ is descending as S/D increases with a sudden reduction in one SP case at $S/D = 1$ and in two SPs at $S/D = 0.5$ with $P/D = 1.5$ and 3. The sudden reduction can be attributed to the base pressure coefficient which will be discussed at the end of this section.

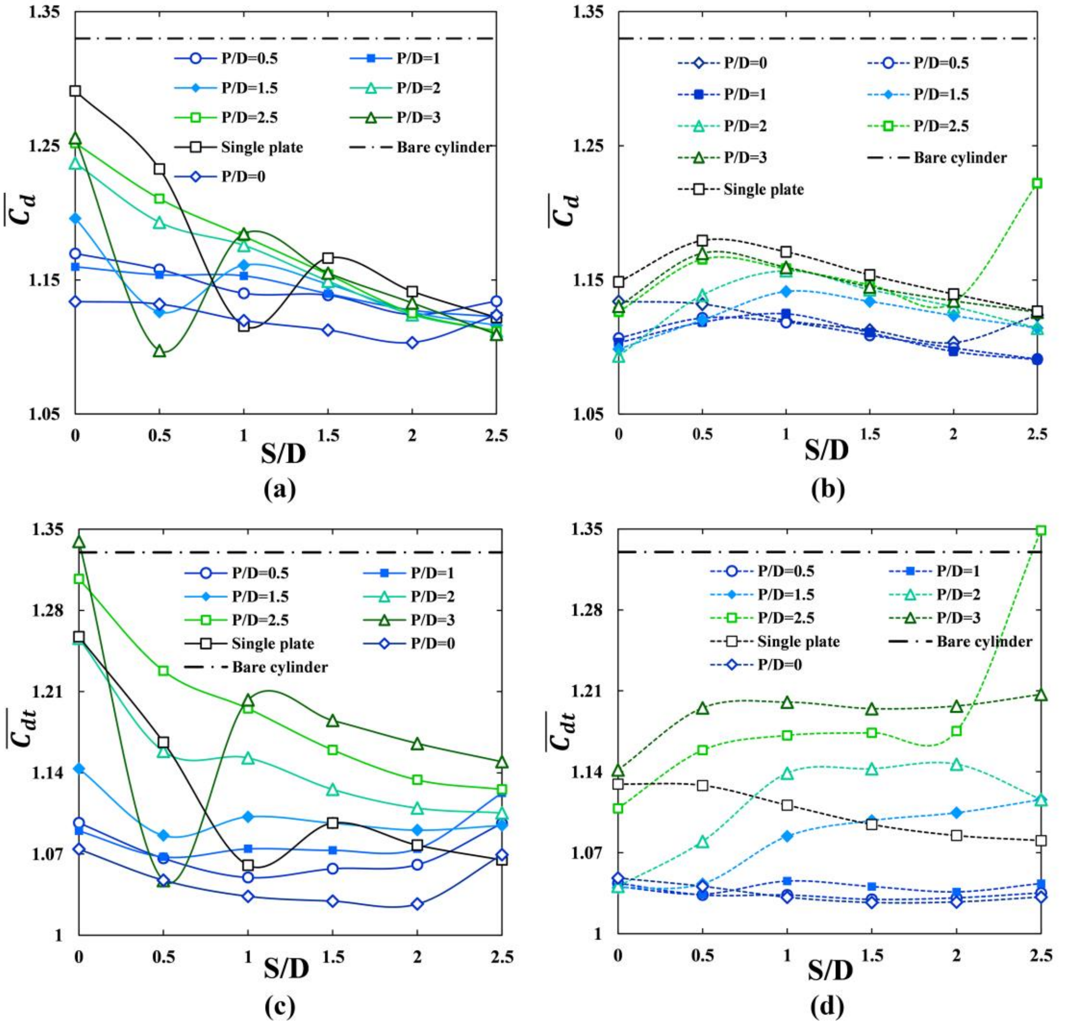

FIG. 10. Variation of the time-averaged drag coefficients against S/D at various P/D: (a) $\overline{C_d}$ in flexible SPs, (b) $\overline{C_d}$ in rigid SPs, (c) $\overline{C_{dt}}$ in flexible SPs, (d) $\overline{C_{dt}}$ in rigid SPs.

For the case of one SP, the rigid SP is more efficient in drag reduction compared to the flexible one except for $S/D = 1$ (Fig. 10 (a)-(b)). That is because in flexible case, two main strong vortices turn into four weaker ones and only two small vortices remain to interact with the cylinder (Fig. 7(b)). Moreover, in some configurations of two SPs, the flexible SPs are more efficient in the $\overline{C_d}$ reduction than the rigid one ($2 \leq P/D \leq 2.5$ and $S/D \geq 2$ and also $P/D = 3$ and $S/D = 0.5$ and 2.5. To clarify the reason for the higher reduction in the flexible SPs cases, the case with $P/D = S/D = 2.5$ is selected for further discussion in which a sudden jump occurs in $\overline{C_d}$ (Fig.10(b)) . Streamlines of this case are shown in Fig.11 for both flexible and rigid SPs. The first rigid SP which is close to the cylinder, modifies the wake structure in such a way that two small vortices are generated at the trailing edge of the first SP and the cylinder vortices cannot significantly grow (Fig.11(b)). However, the cylinder vortices in the flexible cases can grow freely because the first SP moves with the cylinder shear layers. The wake region in the rigid cases has lower pressure and consequently a higher $\overline{C_d}$ is observed in the Fig. 10. For the rigid cases, the minimum of $\overline{C_d}$ occurs in the case with two SPs when $S/D = 2.5$ and $P/D = 0.5$ and 1. In these arrangements, 18% reduction is obtained compared to the bare cylinder. For the flexible cases, the maximum reduction in $\overline{C_d}$ is achieved for the case of two SPs ($S/D = 0.5$ and $P/D = 3$) with 17.48% reductions compared to the bare cylinder~~.~~

The main differences between the $\overline{C_{dt}}$ and $\overline{C_d}$ graphs originated from the viscous drag of the SPs because their pressure drag is not significant. As can be seen in Fig. 10, the trends of $\overline{C_{dt}}$ graph is similar to $\overline{C_d}$ with slightly bigger values which is due to the viscous drag over the SPs. In all cases of flexible and rigid SPs, the value of $\overline{C_{dt}}$ is lower than the bare cylinder except at $S/D = 0$ and $P/D = 3$ in the flexible SPs and $P/D = S/D = 2.5$ in the rigid SPs. The instantaneous dimensionless spanwise vorticity contours (W_z^*) for a half cycle of oscillation in the two cases with higher $\overline{C_{dt}}$ are provided in Fig. 12. For the flexible ones, it can be seen that the main shear layers are under the destructive mechanism with the tip vortex of the first SP. This effect does not let the main vortices of the cylinder to grow significantly and force them to separate faster. In the rigid case (Fig12 (b)), this effect is not existed. However, the first SP, do not let the main cylinder vortices to grow further.

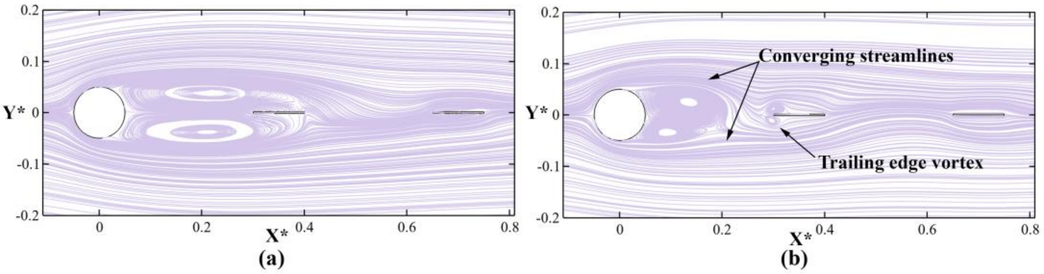

FIG. 11. Time-averaged streamlines for two SPs case at $P/D = S/D = 2.5$: (a) flexible SPs, (b) rigid SPs.

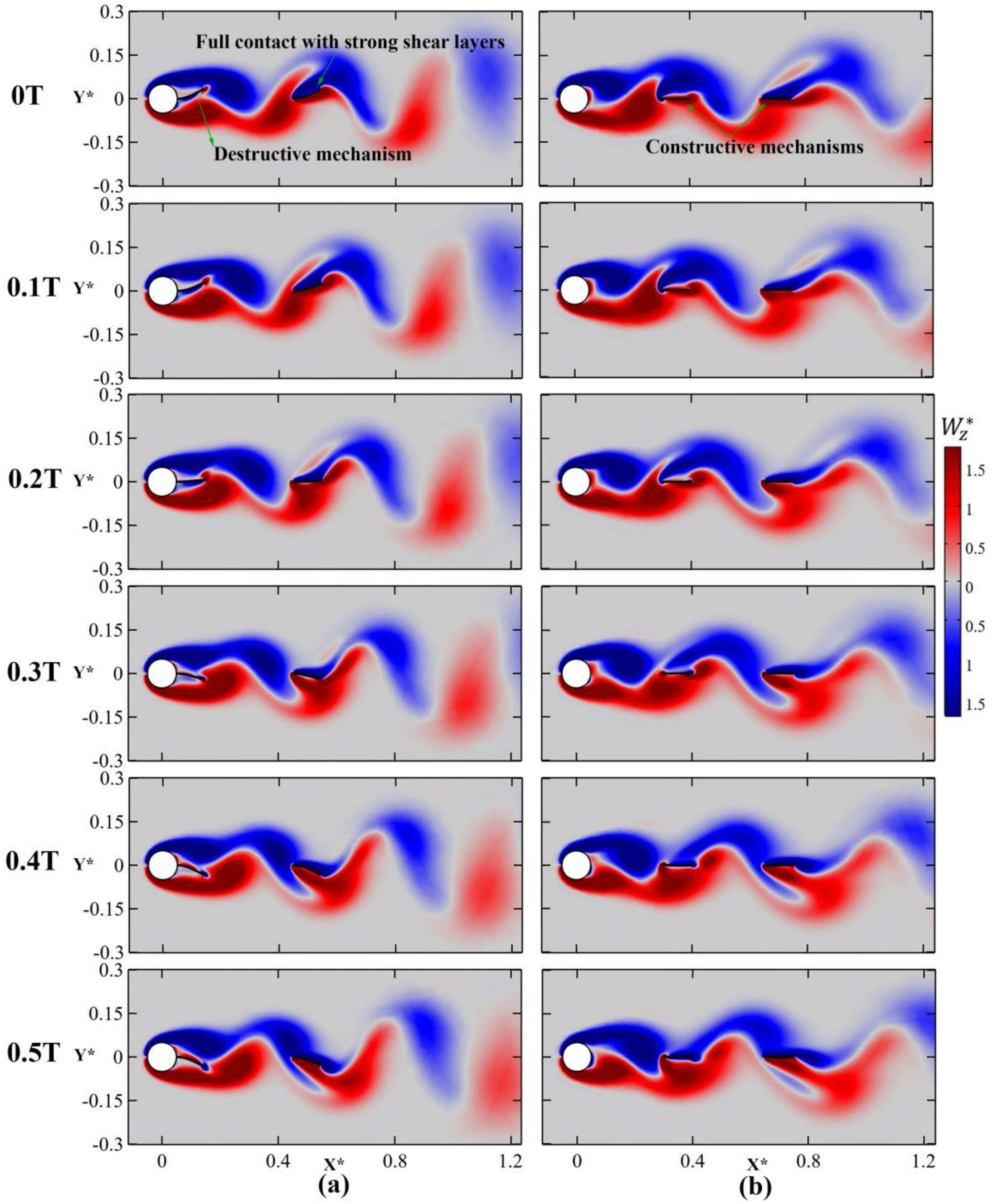

FIG. 12. Instantaneous dimensionless spanwise vorticity contours (W_z^*) for two SPs case (a) flexible SPs at $S/D = 0$ and $P/D = 3.5$, (b) rigid SPs $P/D = S/D = 2.5$.

Fig. 13 presents the variation of RMS of the lift coefficient ($C_{l_{rms}}$) against S/D for the case of flexible SPs. When flow past over a bluff body, vortices which have a low pressure region on their center are shed alternately relative to the wake centerline [62]. Therefore, there is a low-pressure region on one side of the cylinder (vortices side) and a high-pressure region on the other side By shedding vortices, fluctuations in the lift force occur. Hence, the reduction of $C_{l_{rms}}$ is a representative of the wake oscillation. As can be seen, using flexible SPs reduces $C_{l_{rms}}$ dramatically compared to the bare cylinder. There is a noticeable reduction in all cases for $S/D \geq 0.5$ which shows detached SPs have a better performance in terms of $C_{l_{rms}}$reduction compared to the attached ones. Also, it can be seen that $C_{l_{rms}}$ is completely suppressed in one SP at $S/D = 1$ and in two SPs at $0.5 \leq S/D \leq 2$ and $P/D = 0$ as well as $S/D = 0.5$ and

$P/D = 3$. It should be noticed that the variation in $\overline{C_d}$ and $C_{l_{rms}}$ is directly related to the time-averaged pressure coefficient ($\overline{C_P}$), which will be discussed in the next section.

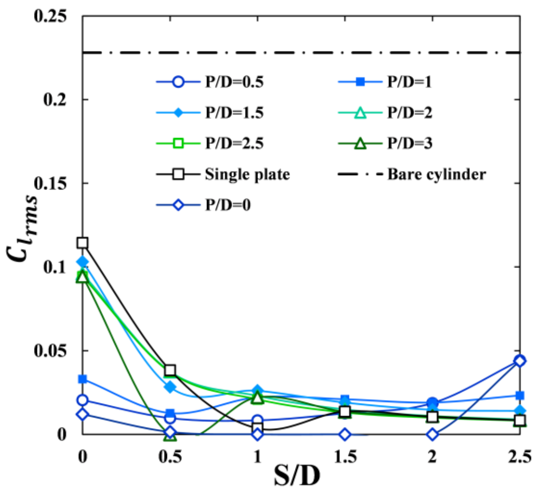

FIG. 13. RMS of the lift coefficient ($C_{l_{rms}}$) at different arrangement of the flexible SPs.

3.4. Pressure coefficient

The variation of $\overline{C_d}$ and $C_{l_{rms}}$ can be justified by the pressure distribution over the cylinder surface. Fig. 14 depicts the symmetric curve of $\overline{C_P}$ in the case of flexible SPs versus angle (θ). The θ is the angle between the centerline of the cylinder and an arbitrary point on the surface of the cylinder. It is defined from the front stagnation point. The $\overline{C_P}$ of the bare cylinder is also plotted in Fig. 14. The trend of $\overline{C_P}$ curve is similar for both cases of flexible SPs and the bare cylinder. In addition, the $\overline{C_P}$ curve shares the same profile at all ratios of S/D and P/D.

The maximum $\overline{C_P}$ occurs at $\theta = 0^{\circ}$ (or 360°), where the flow slows down towards the frontal stagnation point. By increasing θ, the flow accelerates at the upper and lower sides of the cylinder, which causes drop in pressure until reach to the minimum at almost $\theta = 83°$. where the time averaged separation is occurred [63]. After flow separation, $\overline{C_P}$ increases until it reaches the rear stagnation point at $\theta = 180°$. Using SPs slightly increases the pressure in the rear surface of the cylinder. The reason is that the presence of SPs downstream of the cylinder modifies the flow wake and makes appropriate pressure balance on the cylinder surface. So, there would be a significant reduction of the pressure component of the drag and lift coefficient, which leads to lower values of $C_{l_{rms}}$ and $\overline{C_d}$.

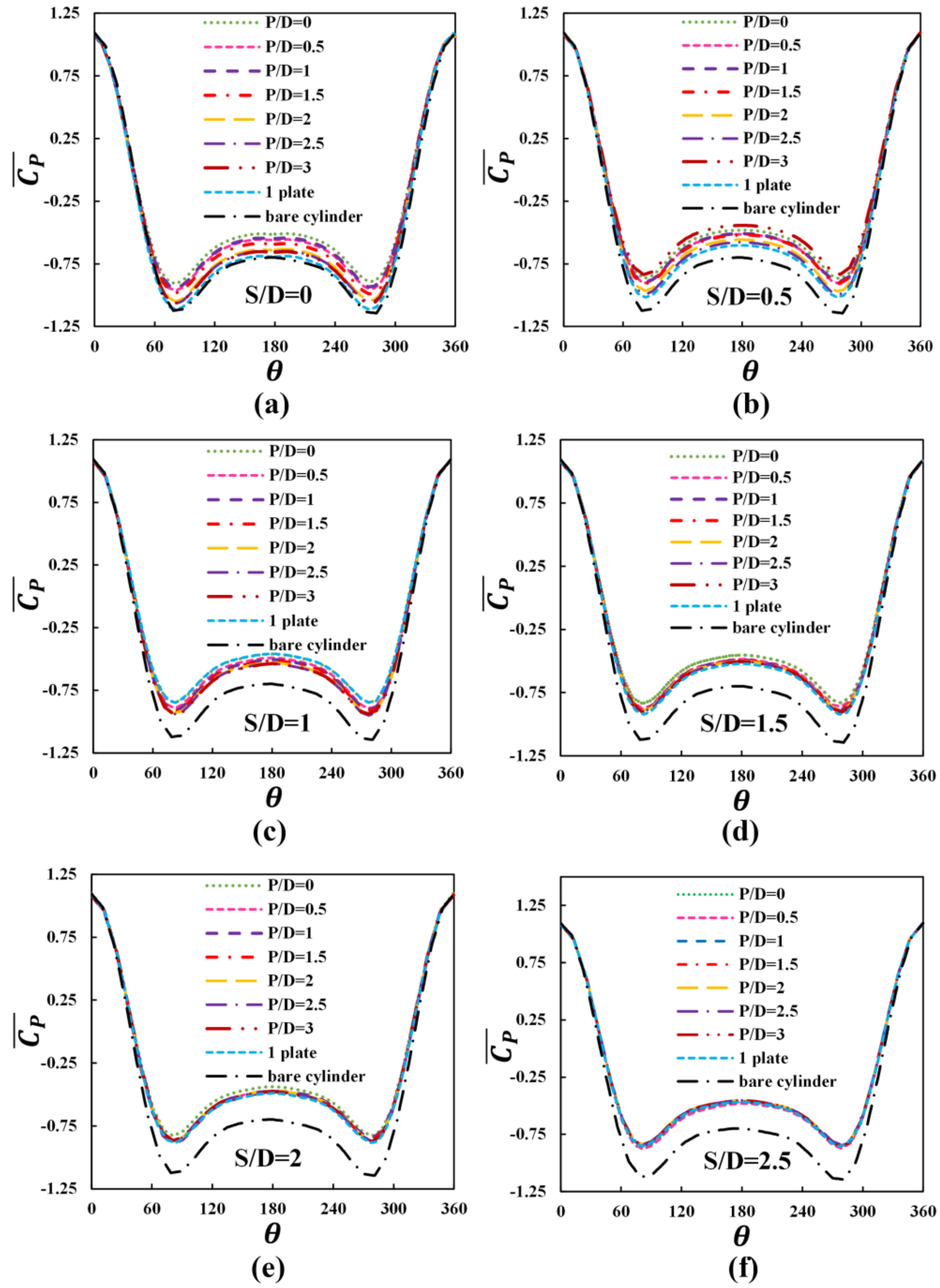

(a) (b) (c) (d) (e) (f)

FIG. 14. The $\overline{C_P}$ distribution for the case of flexible SPs at various S/D and P/D: (a) S/D=0, (b) S/D=0.5, (c) S/D=1, (d) S/D=1.5, (e) S/D=2, (f) S/D=2.5.

If the $\overline{C_P}$ is calculated at $\theta = 180^{\circ}$, the base pressure coefficient would be obtained (equation (18)). Figure 15 indicates the graph of time-averaged base pressure coefficient, which multiplied by (-1) for convenience of analysis ($-\overline{C_{Pb}}$). The value of $-\overline{C_{Pb}}$ for all arrangements of SPs is smaller than the value of the bare cylinder. Since the SPs modifies the flow wake and increase the pressure at the rear stagnation point. Furthermore, it shares almost similar trends with $C_{l_{rms}}$ (Fig. 13) and exactly the same trend with $\overline{C_d}$ (Fig. 10(a)). It proves that the main reason of the lift and drag fluctuations is pressure variation over the cylinder. The sudden drops in $\overline{C_d}$ in Fig. 10(a) can be justified by Fig. 15 where a lower $-\overline{C_{Pb}}$ can be observed in the mentioned points (in one SP case at $S/D = 1$ and in two SPs at $S/D = 0.5$ with $P/D = 1.5$ and 3).

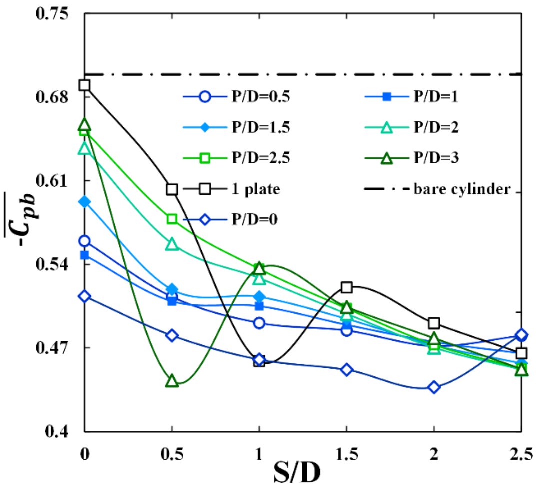

FIG. 15. Time-averaged base pressure coefficient ($-\overline{C_{Pb}}$) at different arrangement of flexible SPs.

3.5. Amplitude of the SPs' fluctuation

The flexible SPs have a periodic deformation due to the continuous local pressure difference across them. The maximum deformation is observed at the tip of the SPs. Fig. 16 illustrates the dimensionless SPs tip amplitude ($A^* = A/D$) for the first and second flexible SPs. Both diagrams share the same trends except for $0.5 \leq P/D \leq 1$. That is because increasing the gap between the SPs (P/D) changes the wake region. In several cases, measurement of the normalized tip amplitude indicates a higher amplitude of the two SP cases compared to the one SP cases in the corresponding arrangements. Comparison of the total normalized tip amplitude shows that the amplitude of the two SPs increases with the ratio of 18.29 compared to the one SP at $S/D = 1$. The maximum value of A^* is observed at the second SP with $S/D = 0$ and $P/D = 2$ due to the appropriate arrangement of the SPs for contacting with shear layers. The same A^* in one SP cases is obtained when the SP is attached to the cylinder ($S/D = 0$). Moreover, the amplitude of the two SPs cases at $1 \leq S/D \leq 2$ and $P/D = 0$ and at $S/D = 0.5$ and $P/D = 3$ are zero, which is inconsistent with $C_{l_{rms}}$ results in Fig. 13. This is related to wake stabilization effect of the SPs which causes vortices became symmetric with respect to the wake centerline. As a result, the SPs are not subject to any resultant force in the perpendicular direction to main flow stream. It should be noted that for a case of one SP, the trends of the St graph (Fig. 6(a)) and A^* graph (Fig. 16(a)) are the same. It can be concluded that higher displacement of the SPs tip leads to increase of the wake instability and results in a higher Strouhal number. However, for the case of two SPs, the behavior of St and SPs amplitudes are different because of the complicated mechanism of VS and the negligible effect of the SPs on cylinder oscillation at further distances.

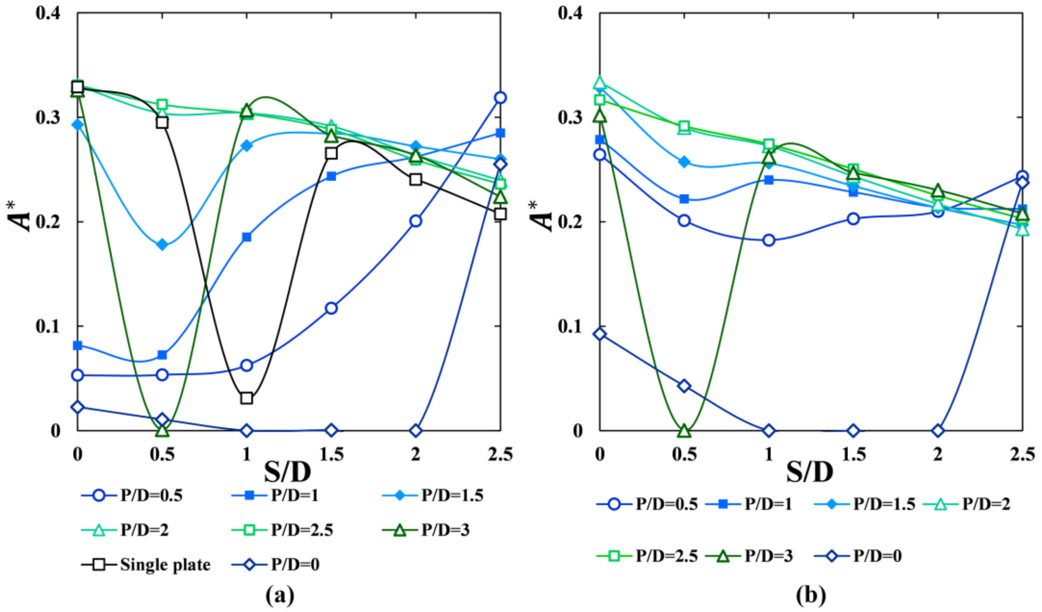

FIG. 16. The non-dimensional tip amplitude (A^*) against S/D at various P/D for the case of flexible SPs: (a) first SP, (b) second SP.

3.6. Strain

The strain is an essential parameter for generating electricity from a piezoelectric polymer. Hence, to harvest more electricity from the flow, the strain (ε) of the SPs should be investigated in detail. In our study, the VS induces strain in the SPs. The maximum strain of flexible SPs (ε_{max}) at various arrangements of SPs is shown in Fig. 17. The corresponding results of one SP case are added to the figure. For the cases of two SPs, the presented strain is the sum of the first SP strain and the second SP strain By performing a parametric study based on gap-ratios (S/D and P/D), the effect of SPs arrangement on strain can be analyzed. As can be seen, in the one SP case, the highest strain occurs at $S/D = 0$. The strain in the case of two SPs is larger than the one SP in several arrangements of SPs. Hence, adding the second SP has a significant effect on increasing the strain and higher energy can be harvested from the flow in the case of two SPs compared to one SP. The highest value of ε_{max} in two SPs case occurs at $1.5 \leq P/D \leq 3$ and $S/D = 0$ which is the best arrangement for locating a piezoelectric polymer. In this range, $P/D = 1.5$ is recommended due to less value of the $\overline{C_d}$.

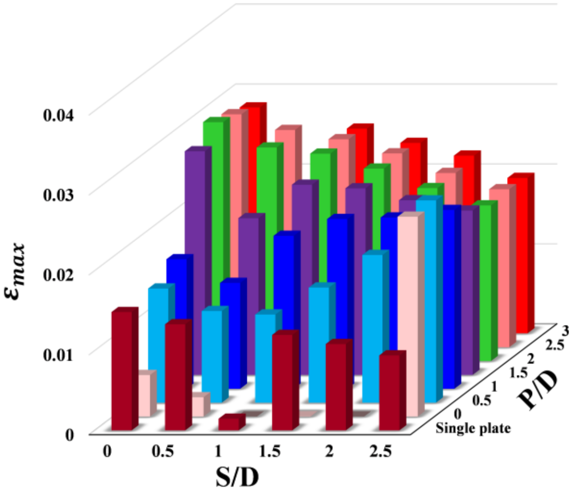

FIG. 17. Variation of maximum strain (ε_{max}) of the flexible SPs against S/D and P/D.

4. Summary and conclusion

In this study, fluid flow over a stationary cylinder at Re = 100 is investigated in the presence of rigid and flexible SPs. The novelty of this work is the use of one and two detached SPs downstream of a cylinder, in which the non-dimensional gap distance between the first SP and cylinder as well as the distance between the SPs are varied. The results of this study can be used energy harvesting by the piezoelectric polymer. A comprehensive parametric study is performed to consider the effect of SPs-cylinder distance as well as the SPs' distance to find the optimal design for energy harvesting. To the best of authors' knowledge, there is no inclusive study in literature that aims at minimizing the unwanted wake effects, while maximizing the harvested energy simultaneously. To make such an assessment, the drag and pressure coefficients as well as the Strouhal number are evaluated. The tip amplitude and strain of the flexible SP are calculated and the optimal arrangement of SPs for installing a piezoelectric polymer are obtained ($S/D = 0$ and $P/D = 1.5$). It is found that the maximum decrease in the St occurs at $S/D = 1.5$ and $P/D = 0$ for both cases of rigid and flexible SPs. The arrangement of SPs results in a reduction of 97.8% and 76.35% for rigid and flexible cases compared to the bare cylinder, respectively. The results also reveal that the rigid and flexible SPs can successfully suppress the VS. However, the performance of rigid SPs is more effective than the flexible SPs for eliminating the VS. Results indicate that the St, $\overline{C_d}$, $\overline{C_P}$ can be controlled significantly by using detached SPs in certain arrangements. In addition, changing the location of the SPs varies the strain in the SPs and can lead to different amounts of electricity generation with piezoelectric polymer. With regards to the current worldwide energy demands, and transition into clean energy, the use of such flexible SPs provides considerable benefits over the typical cylindrical structure for energy harvesting. An efficient design of a cylindrical structure for energy harvesting with significant applications in industry can be a potential topic of future research in this area.

Funding

This research did not receive any specific grant from funding agencies in the public, commercial, or not-for-profit sectors.

Conflict of interest

The authors declare that they have no conflict of interest.

ORCID iDs

Faezeh Eydi https://orcid.org/0000-0002-7701-0317
Afsaneh Mojra https://orcid.org/0000-0001-8790-7016
Rezvan Abdi https://orcid.org/0000-0002-1015-050X

Data availability

The data that support the findings of this study are available from the corresponding author upon reasonable request.

References

1. Dong, S., G. Triantafyllou, and G. Karniadakis, *Elimination of vortex streets in bluff-body flows.* Physical review letters, 2008. **100**(20): p. 204501.
2. Liu, Z.-h., et al., *Numerical simulation and experimental study of the new method of horseshoe vortex control.* Journal of Hydrodynamics, 2010. **22**(4): p. 572-581.
3. Ma, R., et al., *Control of Aeolian tones from a circular cylinder using forced oscillation.* Aerospace Science and Technology, 2019. **94**: p. 105370.
4. Sudhakar, Y. and S. Vengadesan, *Vortex shedding characteristics of a circular cylinder with an oscillating wake splitter plate.* Computers & Fluids, 2012. **53**: p. 40-52.
5. Choi, H., W.-P. Jeon, and J. Kim, *Control of flow over a bluff body.* Annu. Rev. Fluid Mech., 2008. **40**: p. 113-139.
6. Dutton, R. and N. Isyumov, *Reduction of tall building motion by aerodynamic treatments.* Journal of Wind Engineering and Industrial Aerodynamics, 1990. **36**: p. 739-747.
7. Abdi, R., N. Rezazadeh, and M. Abdi, *Reduction of fluid forces and vortex shedding frequency of a circular cylinder using rigid splitter plates.* European Journal of Computational Mechanics, 2017. **26**(3): p. 225-244.
8. Abdi, R., N. Rezazadeh, and M. Abdi, *Investigation of passive oscillations of flexible splitter plates attached to a circular cylinder.* Journal of Fluids and Structures, 2019. **84**: p. 302-317.
9. Zhu, H., et al., *Numerical evaluation of the suppression effect of a free-to-rotate triangular fairing on the vortex-induced vibration of a circular cylinder.* Applied Mathematical Modelling, 2017. **52**: p. 709-730.
10. Hasheminejad, S.M. and Y. Masoumi, *Hybrid active flow induced vibration control of a circular cylinder equipped with a wake-mounted smart piezoelectric bimorph splitter plate.* Journal of Fluids and Structures, 2022. **110**: p. 103531.

11. D. Gao et al., “Review of the excitation mechanism and aerodynamic flow control of vortex-induced vibration of the main girder for long-span bridges: A vortex-dynamics approach,” J. Fluids Struct. 105, 103348 (2021).

12. Gao, D., et al., *Review of the excitation mechanism and aerodynamic flow control of vortex-induced vibration of the main girder for long-span bridges: A vortex-dynamics approach.* Journal of Fluids and Structures, 2021. **105**: p. 103348.

13. Hong, K.-S. and U.H. Shah, *Vortex-induced vibrations and control of marine risers: A review.* Ocean Engineering, 2018. **152**: p. 300-315.

14. Souri, M. and A. Mojra, *A nexus between active and passive control methods for reduction of aerodynamic noise of circular cylinder.* International Journal of Mechanical Sciences, 2021. **200**: p. 106446.

15. Assi, G.R.d.S., R.M. Orselli, and M. Silva-Ortega, *Control of vortex shedding from a circular cylinder surrounded by eight rotating wake-control cylinders at Re= 100.* Journal of Fluids and Structures, 2019. **89**: p. 13-24.

16. Abbasi, S. and M. Souri, *Reducing aerodynamic noise in a rod-airfoil using suction and blowing control method.* International Journal of Applied Mechanics, 2020. **12**(04): p. 2050036.

17. Rastan, M., et al., *Controlled flow over a finite square cylinder using suction and blowing.* International Journal of Mechanical Sciences, 2019. **156**: p. 410-434.

18. Yu, H., et al., *Wake stabilization behind a cylinder by secondary flow over the leeward surface.* Physics of Fluids, 2022. **34**(5): p. 055110.

19. Meng, H., et al., *Characteristics of forced flow past a square cylinder with steady suction at leading-edge corners.* Physics of Fluids, 2022. **34**(2): p. 025119.

20. Kim, S.-J. and C.M. Lee, *Investigation of the flow around a circular cylinder under the influence of an electromagnetic force.* Experiments in fluids, 2000. **28**(3): p. 252-260.

21. Wang, C., et al., *Control of wakes and vortex-induced vibrations of a single circular cylinder using synthetic jets.* Journal of Fluids and Structures, 2016. **60**: p. 160-179.

22. Gao, D., et al., *Active flow control of the dynamic wake behind a square cylinder using combined jets at the front and rear stagnation points.* Physics of Fluids, 2021. **33**(4): p. 047101.

23. Kim, M., E. Essel, and P. Sullivan, *Effect of varying frequency of a synthetic jet on flow separation over an airfoil.* Physics of Fluids, 2022. **34**(1): p. 015122.

24. Bao, Z., et al., *Numerical investigation of flow around a slotted circular cylinder at low Reynolds number.* Journal of Wind Engineering and Industrial Aerodynamics, 2018. **183**: p. 273-282.

25. Sharma, B. and R. Barman, *Steady laminar flow past a slotted circular cylinder.* Physics of Fluids, 2020. **32**(7): p. 073605.

26. Apelt, C., G. West, and A.A. Szewczyk, *The effects of wake splitter plates on the flow past a circular cylinder in the range 104< R< 5× 104.* Journal of Fluid Mechanics, 1973. **61**(1): p. 187-198.

27. Gerrard, J., *The mechanics of the formation region of vortices behind bluff bodies.* Journal of fluid mechanics, 1966. **25**(2): p. 401-413.

28. Roshko, A., *On the drag and shedding frequency of two-dimensional bluff bodies.* 1954.

29. Unal, M. and D. Rockwell, *On vortex formation from a cylinder. Part 2. Control by splitter-plate interference.* Journal of Fluid Mechanics, 1988. **190**: p. 513-529.

30. Zhang, K., et al., *Numerical study on the effect of shape modification to the flow around circular cylinders.* Journal of Wind Engineering and Industrial Aerodynamics, 2016. **152**: p. 23-40.

31. Yang, Q., et al., *Modification of aerodynamic force characteristics on high-rise buildings with arrangement of vertical plates.* Journal of Wind Engineering and Industrial Aerodynamics, 2020. **200**: p. 104155.
32. Wang, J., et al., *Aerodynamic performance of a grooved cylinder in flow conditions encountered by bridge stay cables in service.* Journal of Wind Engineering and Industrial Aerodynamics, 2019. **188**: p. 80-89.
33. Bearman, P. and J. Harvey, *Control of circular cylinder flow by the use of dimples.* AIAA journal, 1993. **31**(10): p. 1753-1756.
34. Derakhshandeh, J.F. and N. Gharib, *Numerical investigations on the flow control over bumped surface circular cylinders.* Ocean Engineering, 2021. **240**: p. 109943.
35. Mishra, A., M. Hanzla, and A. De, *Passive control of the onset of vortex shedding in flow past a circular cylinder using slit.* Physics of Fluids, 2020. **32**(1): p. 013602.
36. Kwon, K. and H. Choi, *Control of laminar vortex shedding behind a circular cylinder using splitter plates.* Physics of Fluids, 1996. **8**(2): p. 479-486.
37. Sharma, K. and S. Dutta, *Flow control over a square cylinder using attached rigid and flexible splitter plate at intermediate flow regime.* Physics of Fluids, 2020. **32**(1): p. 014104.
38. Shukla, S., R. Govardhan, and J. Arakeri, *Flow over a cylinder with a hinged-splitter plate.* Journal of Fluids and Structures, 2009. **25**(4): p. 713-720.
39. Amiraslanpour, M., J. Ghazanfarian, and S.E. Razavi, *Drag suppression for 2D oscillating cylinder with various arrangement of splitters at Re= 100: a high-amplitude study with OpenFOAM.* Journal of Wind Engineering and Industrial Aerodynamics, 2017. **164**: p. 128-137.
40. Hwang, J.-Y. and K.-S. Yang, *Drag reduction on a circular cylinder using dual detached splitter plates.* Journal of wind engineering and industrial aerodynamics, 2007. **95**(7): p. 551-564.
41. Bao, Y. and J. Tao, *The passive control of wake flow behind a circular cylinder by parallel dual plates.* Journal of Fluids and Structures, 2013. **37**: p. 201-219.
42. Ozkan, G.M., E. Firat, and H. Akilli, *Passive flow control in the near wake of a circular cylinder using attached permeable and inclined short plates.* Ocean Engineering, 2017. **134**: p. 35-49.
43. Zhu, H. and W. Liu, *Flow control and vibration response of a circular cylinder attached with a wavy plate.* Ocean Engineering, 2020. **212**: p. 107537.
44. Gao, D., et al., *Modification of subcritical cylinder flow with an upstream rod.* Physics of Fluids, 2022. **34**(1): p. 015107.
45. Ramadan, K.S., D. Sameoto, and S. Evoy, *A review of piezoelectric polymers as functional materials for electromechanical transducers.* Smart Materials and Structures, 2014. **23**(3): p. 033001.
46. Shukla, S., R. Govardhan, and J. Arakeri, *Dynamics of a flexible splitter plate in the wake of a circular cylinder.* Journal of Fluids and Structures, 2013. **41**: p. 127-134.
47. Wu, J., C. Shu, and N. Zhao, *Numerical study of flow control via the interaction between a circular cylinder and a flexible plate.* Journal of Fluids and Structures, 2014. **49**: p. 594-613.
48. Sun, X., et al., *Dynamics of a circular cylinder with an attached splitter plate in laminar flow: A transition from vortex-induced vibration to galloping.* Physics of Fluids, 2020. **32**(2): p. 027104.
49. Chehreh, B.B. and K. Javadi, *Flow control around a circular cylinder with swinging thin plates.* Journal of Fluids and Structures, 2018. **81**: p. 738-760.

50. Pfister, J.-L. and O. Marquet, *Fluid–structure stability analyses and nonlinear dynamics of flexible splitter plates interacting with a circular cylinder flow.* Journal of Fluid Mechanics, 2020. **896**.
51. Turek, S. and J. Hron, *Proposal for numerical benchmarking of fluid-structure interaction between an elastic object and laminar incompressible flow*, in *Fluid-structure interaction*. 2006, Springer. p. 371-385.
52. Donea, J., et al., *Arbitrary L agrangian–E ulerian Methods.* Encyclopedia of computational mechanics, 2004.
53. Díaz-Ojeda, H., L. González, and F. Huera-Huarte, *On the influence of the free surface on a stationary circular cylinder with a flexible splitter plate in laminar regime.* Journal of Fluids and Structures, 2019. **87**: p. 102-123.
54. Knupp, P.M., *Winslow smoothing on two-dimensional unstructured meshes.* Engineering with Computers, 1999. **15**(3): p. 263-268.
55. Zhu, H. and T. Zhou, *Flow around a circular cylinder attached with a pair of fin-shaped strips.* Ocean Engineering, 2019. **190**: p. 106484.
56. Zhu, H., W. Liu, and T. Zhou, *Direct numerical simulation of the wake adjustment and hydrodynamic characteristics of a circular cylinder symmetrically attached with fin-shaped strips.* Ocean Engineering, 2020. **195**: p. 106756.
57. Jiang, H., et al., *Two-and three-dimensional instabilities in the wake of a circular cylinder near a moving wall.* Journal of Fluid Mechanics, 2017. **812**: p. 435-462.
58. Norberg, C., *Fluctuating lift on a circular cylinder: review and new measurements.* Journal of Fluids and Structures, 2003. **17**(1): p. 57-96.
59. Williamson, C.H., *Oblique and parallel modes of vortex shedding in the wake of a circular cylinder at low Reynolds numbers.* Journal of Fluid Mechanics, 1989. **206**: p. 579-627.
60. Abdi, R., M. Krzaczek, and J. Tejchman, *Comparative study of high-pressure fluid flow in densely packed granules using a 3D CFD model in a continuous medium and a simplified 2D DEM-CFD approach.* Granular Matter, 2022. **24**(1): p. 1-25.
61. Younis, M., M. Alam, and Y. Zhou, *Flow around two non-parallel tandem cylinders.* Physics of Fluids, 2016. **28**(12): p. 125106.
62. Roshko, A., *On the drag and shedding frequency of two-dimensional bluff bodies*. 1954.
63. Zdravkovich, M.M., *Flow around circular cylinders: Volume 2: Applications*. Vol. 2. 1997: Oxford university press.